

Screening and activation of two-dimensional MA_2Z_4 for hydrogen evolution reaction: A first-principles study

Meng Tian(田萌)

Citation: Chin. Phys. B. 35, 098801 (2026). DOI: 10.1088/1674-1056/ae2bf1 |
CSTR: 32038.14.CPB.ae2bf1
http://cpb.iphy.ac.cn; http://iopscience.iop.org/cpb

What follows is a list of articles you may be interested in

Enhancement of hydrogenation kinetics and thermodynamic properties of $ZrCo_{1-x}Cr_x$ (x= 0-0.1) alloys for hydrogen storage

Linling Luo(罗林龄), Xiaoqiu Ye(叶小球), Guanghui Zhang(张光辉), Huaqin Kou(寇化秦), Renjin Xiong(熊仁金), Ge Sang(桑革), Ronghai Yu(于荣海), Dongliang Zhao(赵栋梁)
Chin. Phys. B. 29, 088801 (2020). DOI: 10.1088/1674-1056/ab9289

An overview of progress in Mg-based hydrogen storage films

Lyu Jinzhe, Andrey M Lider, Viktor N Kudiiarov
Chin. Phys. B. 28, 098801 (2019). DOI: 10.1088/1674-1056/ab33f0

Dissociation of H_2 on Mg-coated $B_{12}C_6N_6$

Li Ma(马丽), Xue-Ling Jin(金雪玲), Hui-Hui Yang(杨慧慧), Xiao-Xia Wang(王小霞), Ning Du(杜宁), Hong-Shan Chen(陈宏善)
Chin. Phys. B. 26, 068801 (2017). DOI: 10.1088/1674-1056/26/6/068801

Screening and activation of two-dimensional MA_2Z_4 for hydrogen evolution reaction: A first-principles study

Meng Tian(田萌)†

School of New Energy, Nanjing University of Science and Technology, Jiangyin 214443, *China*

(Received 24 September 2025; revised manuscript received 9 December 2025; accepted manuscript online 12 December 2025)

Developing efficient and low-cost catalysts for the hydrogen evolution reaction (HER) is crucial for sustainable hydrogen production. This study focuses on the novel two-dimensional MA_2Z_4 material family (M = transition metal, A = Si/Ge, Z = N/P/As). We systematically screened structurally stable MA_2Z_4 materials for HER activity and developed activation strategies for inert variants. Six compounds ($ZrSi_2N_4$, $ZrGe_2N_4$, $NbSi_2N_4$, $TaGe_2N_4$, $NbGe_2N_4$, $HfGe_2N_4$) exhibit outstanding HER performance, characterized by near-zero hydrogen adsorption free energy and high exchange current densities. Furthermore, doping inert WGe_2N_4 with specific elements (e.g., Ru, Re, Hf, Cu) effectively activates its HER performance. This enhancement stems from strengthened N–H bonding due to N_{2p_z} and H_{1s} orbital hybridization in doped configurations. The work provides strategies for designing high-performance two-dimensional (2D) MA_2Z_4 HER catalysts.

Keywords: hydrogen storage, catalysis, first-principles calculations, energy conservation

PACS: 88.30.R–, 82.45.Jn, 68.43.Bc, 88.05.Gh

DOI: 10.1088/1674-1056/ae2bf1 **CSTR:** 32038.14.CPB.ae2bf1

1. Introduction

Hydrogen energy has garnered significant attention due to its environmentally friendly nature, renewability, and high energy density.[1–3] Electrochemical water splitting is an efficient and sustainable technology for hydrogen generation, and its key reaction is the hydrogen evolution reaction (HER).[4,5] HER involves hydrogen chemisorption and the combination of proton-electron pairs. Catalysts are employed to reduce the HER energy barrier and promote HER activity, such as Pt and Pt-based catalysts.[6–8] However, the low abundance and high cost of such noble metals hinder their widespread application. Thus, exploring low-cost and highly effective catalysts is vital for HER. Two-dimensional (2D) materials have attracted great attention due to their diverse chemical properties and abundant active sites, such as transition metal dichalcogenides (TMDs),[9–11] transition metal carbides/nitrides (MXenes),[12–14] and g-C_3N_4.[15] Despite significant efforts, few suitable 2D candidates satisfy all criteria for practical applications. Therefore, it is of great importance to explore suitable 2D HER catalysts.

Recently, a family of 2D MA_2Z_4 materials was discovered in 2020,[16] where M represents a transition metal such as Mo, V, W, etc., A is Si or Ge, and Z stands for N, P, or As.[16,17] MA_2Z_4 crystal structures crystallize in the hexagonal system and consist of septuple Z–A–Z–M–Z–A–Z atomic layers. $MoSi_2N_4$ and WSi_2N_4 have been successfully synthesized using chemical vapor deposition.[16] These two materials have drawn great attention due to their excellent stability and high carrier mobility, exhibiting properties such as piezoelectricity in $MoSi_2N_4$ and promising electrocatalysis in both $MoSi_2N_4$ and WSi_2N_4.[18–22] Moreover, first-principles calculations have predicted properties and potential applications for a series of MA_2Z_4 materials.[23–27] For example, Liu and coworkers found that $TiGe_2P_4$ might be a potential HER catalyst due to its near-zero Gibbs free energy for hydrogen adsorption (ΔG_{*H}).[28] However, the structural stabilities of these systems have not been fully explored. Moreover, few activation strategies have been proposed for HER-inert MA_2N_4 materials. Consequently, it is imperative to conduct an HER activity screening among structurally stable MA_2N_4 materials and develop modification approaches for catalytically inert variants.

In this work, a systematic study was conducted to screen HER catalysts among structurally stable MA_2N_4 materials and develop strategies to trigger HER activity in catalytically inert materials. Six materials ($ZrSi_2N_4$, $ZrGe_2N_4$, $NbSi_2N_4$, $TaGe_2N_4$, $NbGe_2N_4$, and $HfGe_2N_4$) stand out for their near-zero ΔG_{*H} values and excellent exchange current densities. Taking WGe_2N_4 as a representative material with inert HER activity, its HER performance can be effectively activated through doping with Ru, Re, Hf, Cu, Zn, Os, Cd, Fe, and Sc, resulting in superior HER performance. Compared with the pristine WGe_2N_4, the enhanced N–H bonding, resulting from hybridization between N_2p_z and H_1s orbitals in the doped configurations, contributes to their outstanding HER activity. These findings offer a pathway for the rational design of HER catalysts and promote the potential applications of 2D MA_2N_4

†Corresponding author. E-mail: tianmeng@njust.edu.cn

© 2026 Chinese Physical Society and IOP Publishing Ltd. All rights, including for text and data mining, AI training, and similar technologies, are reserved.

materials.

2. Computational method

Density functional theory (DFT) calculations were performed with the Vienna *ab initio* simulation package (VASP).[29] The pseudopotentials of atomic cores were computed using the projector-augmented wave (PAW) method, and the exchange–correlation functional was calculated using the Perdew–Burke–Ernzerhof (PBE) functional.[30] All MA_2Z_4 (M represents a transition metal, A stands for Si or Ge, and Z is N, P, or As) models were built with 15-Å vacuum thickness to avoid interactions between layers. The DFT + D3 method was applied to compute the energy correction term for van der Waals dispersion.[31] Spin-orbit coupling (SOC) was taken into consideration during all structural relaxation and electronic calculations. Transition metal doping was performed through the element substitution method, and all doped systems were rigorously optimized. The cutoff energy of the plane wave was set to 450 eV, and the threshold values for energy and force convergence were 10^{-5} eV and 0.01 eV/Å, respectively. The Brillouin zones were sampled with $21 \times 21 \times 1$ and $3 \times 3 \times 1$ K-point meshes using the Monkhorst–Pack scheme for unit cells and 3×3 supercells, respectively. The J. K. Nørskov model was employed to compute the HER.[32] The Gibbs free energy of the species was calculated by considering entropy and zero-point energy corrections at 298 K. The Gibbs free energy of the H intermediate was computed as half that of hydrogen (H_2). The Gibbs free energy of H adsorption was calculated with the following expression:

$$\Delta G_{*\mathrm{H}} = \Delta E_{*\mathrm{H}} + \Delta E_{\mathrm{ZPE}} - T\Delta S_{*\mathrm{H}},$$

where $\Delta E_{*\mathrm{H}}$, ΔE_{ZPE}, T, and $\Delta S_{*\mathrm{H}}$ represent the free energy of H adsorption, zero-point energy, temperature, and entropy correction, respectively. The hydrogen evolution exchange current density (i) was computed to evaluate the rate of hydrogen evolution on the catalyst surface, using the following equation:

$$i = -\frac{ek_0}{1+\exp\left(\frac{|\Delta G_{*\mathrm{H}}|}{k_{\mathrm{B}}T}\right)},$$

where e, k_0, and k_{B} stand for the elementary charge, rate constant, and Boltzmann constant, respectively, and k_0 was set as 200 s^{-1} site^{-1}.[32] The chemical bonding mechanism of the H–N bond was analyzed with projection density of states (PDOS) and crystal orbital Hamilton population (COHP) methods.[33] The crystal structures were visualized with the electronic and structural analysis (VESTA) software.[34] Formation energies were computed based on the energy difference between MA_2Z_4 and competing structures. Density functional perturbation theory (DFPT)[35] was used to calculate phonon dispersion spectra with $4 \times 4 \times 1$ supercells and $3 \times 3 \times 1$ q grids. The *ab initio* molecular dynamics (AIMD) simulation at 300 K, lasting 5000 fs with a time step of 1 fs, was conducted to verify the dynamic stability.

3. Results and discussion

3.1. Crystal structures of 2D MA_2Z_4

Since MA_2Z_4 monolayers with a septuple-atomic-layer structure can be constructed by intercalating a MZ_2 layer into an A_2Z_2 monolayer, the types of phases for MZ_2 and A_2Z_2 determine the crystal structures of MA_2Z_4 monolayers. Based on the hexagonal MZ_2 and two phases (α and β) of A_2Z_2, the structures of MA_2Z_4 can be classified into four phases: α, β, γ, and δ. A total of 48 compounds were identified with both thermodynamic and dynamic stability from first-principles calculations.[16] There are 13, 15, and 20 compounds belonging to the α_1, α_2, and β_2 phases, respectively. Structural stability is an essential prerequisite for materials research and serves as the physical and chemical foundation of materials. Therefore, these 48 structurally stable compounds were considered in this work.

Figure 1(a) shows three representative crystal structures of MA_2Z_4 (α_1, α_2, and β_2 phases) within the hexagonal crystal system. The hexagonal system and sequence of atomic layers remain the same; however, there are some differences in the atomic positions. According to the crystal symmetry of the hexagonal lattice, three potential sites for hydrogen adsorption were considered: Site I above an A (Si or Ge) atom, Site II above the middle M atom, and Site III above a surface Z (N, P, or As) atom (Fig. 1(b)). For these 48 MA_2Z_4 compounds, they were numbered 1–48 as VSi_2N_4, $NbSi_2N_4$, $TaSi_2N_4$, $NbGe_2N_4$, $TaGe_2N_4$, VSi_2P_4, $NbSi_2P_4$, $TaSi_2P_4$, $CrSi_2N_4$, $MoSi_2N_4$, WSi_2N_4, $MoGe_2N_4$, WGe_2N_4, VGe_2P_4, $NbGe_2P_4$, $TaGe_2P_4$, VSi_2As_4, $NbSi_2As_4$, $TaSi_2As_4$, VGe_2As_4, $NbGe_2As_4$, $TaGe_2As_4$, $CrSi_2P_4$, $MoSi_2P_4$, WSi_2P_4, $CrGe_2P_4$, $MoGe_2P_4$, WGe_2P_4, $ZrSi_2N_4$, $HfSi_2N_4$, $ZrGe_2N_4$, $HfGe_2N_4$, $TiSi_2P_4$, $ZrSi_2P_4$, $HfSi_2P_4$, $TiGe_2P_4$, $ZrGe_2P_4$, $HfGe_2P_4$, $TiSi_2As_4$, $ZrSi_2As_4$, $HfSi_2As_4$, $TiGe_2As_4$, $ZrGe_2As_4$, $HfGe_2As_4$, $MoSi_2As_4$, WSi_2As_4, $MoGe_2As_4$, and WGe_2As_4, respectively. First-principles calculations show that Site III has the lowest $\Delta G_{*\mathrm{H}}$ among the three adsorption sites in the α_1 and β_2 phases, while either Site II or Site III has the most favorable hydrogen adsorption energy (Fig. 1(c)). These results indicate that hydrogen preferentially adsorbs on the surface Z atom rather than above the Si or Ge atom, which could be attributed to the stronger affinity between H and Z atoms than between H and Si or Ge atoms. The lowest-energy configuration for each compound was adopted for the subsequent studies.

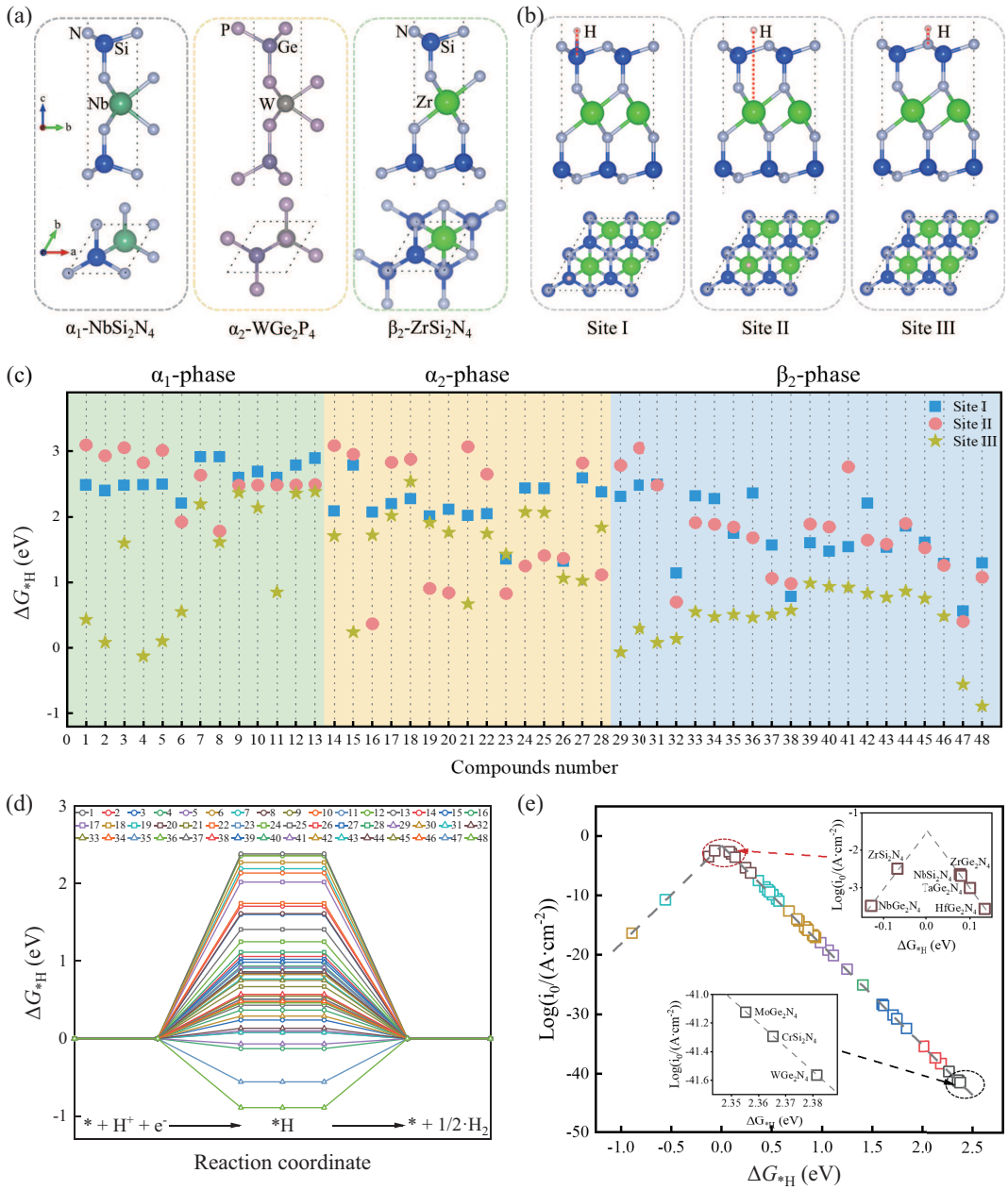


Fig. 1. (a) Crystal structures of α_1-MA_2Z_4, α_2-MA_2Z_4, and β_2-MA_2Z_4. (b) Three potential H adsorption sites. (c) ΔG_{*H} for 48 MA_2Z_4 compounds. (d) Free energy diagram for HER. (e) Volcano curve of exchange current density versus ΔG_{*H} for 48 MA_2Z_4 materials. The embedded figures display the top-performing and lowest-performing current density samples, respectively.

3.2. HER performance

Then, ΔG_{*H} and volcano curve calculations were conducted to provide an intuitive depiction of the HER activity of the catalysts. The HER process consists of two steps: the first step involves hydrogen adsorption onto the catalyst surface, followed by the second step of hydrogen gas evolution. The ΔG_{*H} value was computed according to the chemisorption energy of hydrogen. The ΔG_{*H} values for electrocatalysts below zero represent too strong chemisorption, while values well above zero represent too weak chemisorption of hydrogen. Figure 1(d) shows the variation in ΔG_{*H} across different MA_2Z_4 compounds. By comparison, only $ZrSi_2N_4$, $NbGe_2N_4$, $MoGe_2As_4$, and WGe_2As_4, four MA_2Z_4 compounds, have negative ΔG_{*H} values of −0.07 eV, −0.13 eV, −0.56 eV, and −0.89 eV, respectively. Others have positive ΔG_{*H} values, indicating relatively weaker hydrogen chemisorption energies. Based on the Sabatier principle, ΔG_{*H} should be close to zero to achieve favorable HER kinetics.[36] Among these 48 compounds, $ZrSi_2N_4$, $ZrGe_2N_4$, $NbSi_2N_4$, $TaGe_2N_4$, $NbGe_2N_4$, and $HfGe_2N_4$ exhibit the ΔG_{*H} values closest to zero, with values of −0.07 eV, 0.08 eV, 0.08 eV, 0.10 eV, −0.13 eV, and 0.13 eV, respectively. These values are superior even to those of representative HER catalysts, such as Pt,[37] MoS_2,[38] and C_3N_4.[39] These ΔG_{*H} values for $NbSi_2N_4$ (0.08 eV), $NbGe_2N_4$ (−0.13 eV), and $TaGe_2N_4$ (0.10 eV) are consistent with the literature values of $NbSi_2N_4$ (0.11 eV), $NbGe_2N_4$ (−0.09 eV), and $TaGe_2N_4$ (0.07 eV).[28] A ΔG_{*H} value close

to zero promotes a thermodynamic equilibrium between hydrogen adsorption and desorption, facilitating a low overpotential and a smooth HER reaction. These results indicate that these six materials might have better electrocatalytic HER activity than Pt and MoS_2, suggesting their potential as candidates for HER.

Following the thermodynamic analysis, we conducted kinetic investigations. The current intensity is defined as the electric charge passing through any cross-section per unit time. Thus, the current (i) can be computed as the following equation:

$$i = -er,$$

where r is the net rate of HER. The adsorption of one H^+ ion requires the concomitant transfer of one electron, with hydrogen adsorbing onto active sites. Therefore, the quantity of adsorbed electrons can be determined by calculating the active site density. It means that the net rate r can be computed as

$$r = k \cdot (1-\theta) \cdot c,$$

where k, θ, and c represent the rate constant, hydrogen coverage, and proton concentration on the catalyst, respectively. Based on statistical mechanics principles, hydrogen adsorption and desorption maintain quasi-stable equilibrium. Therefore, we can derive quantitative relationships through statistical thermodynamic calculations

$$\theta = \frac{K}{1+K},$$

where $K = \exp(-\Delta G_{*\mathrm{H}}/(k_\mathrm{B}T))$, k_B is the Boltzmann constant, and T is the temperature. Thus, by quantifying $\Delta G_{*\mathrm{H}}$, the exchange current density of the HER can be calculated as

$$i = -ek_0 \frac{1}{1+\exp\left(\frac{|\Delta G_{*\mathrm{H}}|}{k_\mathrm{B}T}\right)},$$

where k_0 is the rate constant.[32]

As depicted in Fig. 1(e), there are two branches of the volcano curve as a function of $\Delta G_{*\mathrm{H}}$. For the left branch, the HER rate increases toward the maximum and then decreases with increasing $\Delta G_{*\mathrm{H}}$ toward zero, which can be attributed to the difficulty in the recombination of hydrogen (the second step of HER) and the reduced hydrogen release caused by excessively strong chemisorption of hydrogen. For the right branch, the HER rate decreases with increasing $\Delta G_{*\mathrm{H}}$ due to excessively weak hydrogen chemisorption (the first step of HER). First-principles calculations show that $ZrSi_2N_4$, $ZrGe_2N_4$, $NbSi_2N_4$, $TaGe_2N_4$, $NbGe_2N_4$, and $HfGe_2N_4$, six MA_2Z_4 compounds, have excellent exchange current densities due to their high HER rates and exchange current densities. In contrast, WGe_2N_4, $CrSi_2N_4$, and $MoGe_2N_4$ demonstrate poor exchange current densities due to their weak hydrogen chemisorption and large positive $\Delta G_{*\mathrm{H}}$ values. Overall, most MA_2Z_4 compounds exhibit relatively low HER current densities, primarily constrained by either the first (the right branch) or second (the left branch) reaction step of the HER process. Consequently, enhancing the HER performance of 2D MA_2Z_4 compounds is imperative to advance their practical deployment in hydrogen evolution applications.

3.3. Structural stability

The stability of a material is a prerequisite for its synthesis and catalytic application. Therefore, the stability of $ZrSi_2N_4$, $ZrGe_2N_4$, $HfGe_2N_4$, $NbSi_2N_4$, $NbGe_2N_4$, $TaGe_2N_4$, and WGe_2N_4 is investigated by first-principles calculations. Formation energies were computed according to the energy difference between MA_2N_4 materials and competing structures. As shown in Table S1, $NbSi_2N_4$, $TaGe_2N_4$, and $HfGe_2N_4$, three MA_2N_4 materials, exhibit negative formation energies of -0.756 eV, -0.030 eV, and -0.045 eV per atom, respectively, indicating their thermodynamic stability. Although $ZrSi_2N_4$, $ZrGe_2N_4$, $NbSi_2N_4$, and WGe_2N_4 show positive formation energy values, their small values (< 0.24 eV) imply that these materials can still be successfully synthesized under proper conditions. Then, phonon dispersion spectra calculations were conducted to confirm their dynamic stability. The absence of imaginary frequency modes for these seven MA_2N_4 materials confirms their dynamic stability (Figs. 2 and S1).

3.4. Electronic structure

The electronic structure, referring to the distribution and energy states of electrons within a material, determines its conductivity and physicochemical properties. Therefore, electronic band structures and density of states calculations were performed to evaluate the electronic properties of these 2D materials. The calculations reveal that $ZrSi_2N_4$, $ZrGe_2N_4$, $HfGe_2N_4$, and WGe_2N_4 exhibit semiconducting properties with an indirect bandgap of 1.03 eV, a direct bandgap of 1.20 eV, a direct bandgap of 1.17 eV (Fig. 3), and an indirect bandgap of 1.13 eV (Fig. S2), respectively. However, $NbSi_2N_4$, $NbGe_2N_4$, and $TaGe_2N_4$ display half-metallic characteristics (Fig. 3). These results are consistent with previous work.[17] Notably, the bandgaps of β-$ZrSi_2N_4$ and β-$ZrGe_2N_4$ are 1.03 eV and 1.20 eV, respectively, showing an increasing trend from Si- to Ge-based systems. In contrast, α-WSi_2N_4 and α-WGe_2N_4 exhibit an opposite trend in bandgap evolution compared to the Zr-based materials. This can be attributed to the different crystal phases. The half-metallic character or narrow-bandgap semiconductor properties suggest that these materials possess excellent electronic conductivity, which facilitates rapid kinetics in electrocatalytic reactions.

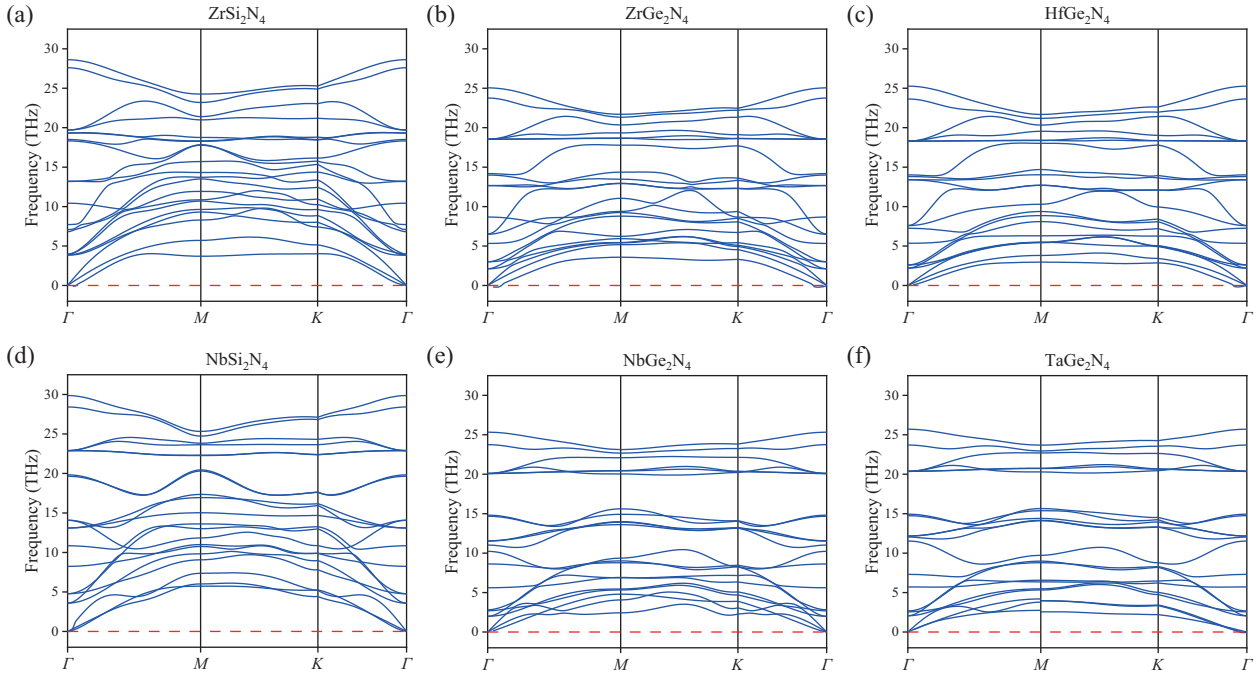


Fig. 2. Calculated phonon dispersion curves of (a) $ZrSi_2N_4$, (b) $ZrGe_2N_4$, (c) $HfGe_2N_4$, (d) $NbSi_2N_4$, (e) $NbGe_2N_4$, and (f) $TaGe_2N_4$.

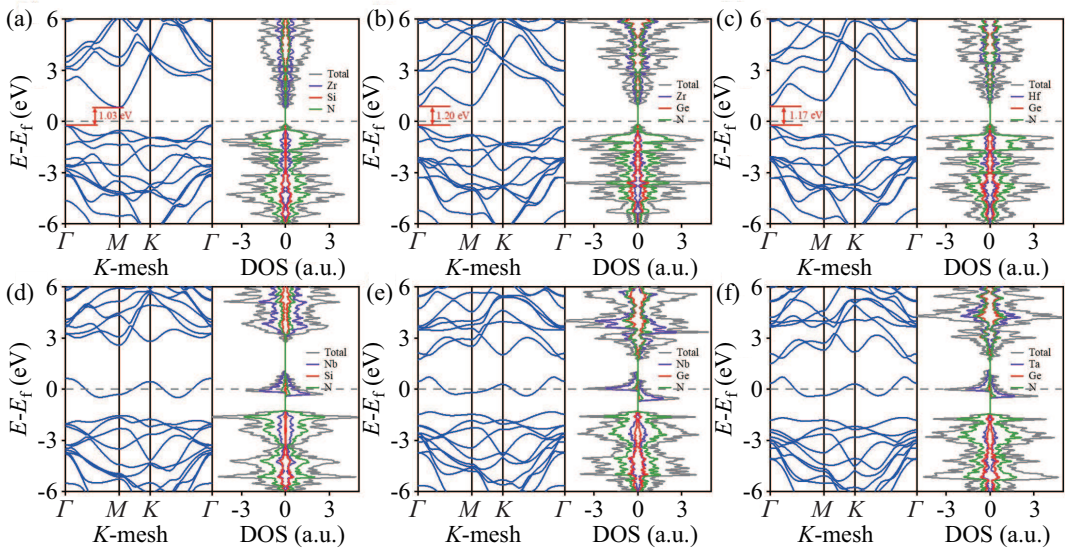


Fig. 3. Electronic band structures and density of states of (a) $ZrSi_2N_4$, (b) $ZrGe_2N_4$, (c) $HfGe_2N_4$, (d) $NbSi_2N_4$, (e) $NbGe_2N_4$, and (f) $TaGe_2N_4$, respectively.

3.5. Activating HER performance of inert MA_2N_4

To activate HER catalytic activity, a doping strategy was adopted by introducing transition metal (TM) dopants. WGe_2N_4 was selected as the representative MA_2N_4 material due to its inert HER activity. In WGe_2N_4, there are four distinct atomic sites, each with a different coordination environment. The variation in atomic sites can influence the electronic structure and physicochemical properties. To gain a more comprehensive understanding of how doping affects the HER performance of MA_2Z_4 materials, we conducted doping at all four atomic sites. As shown in Fig. 4(a), a total of 28 transition metals (3d, 4d, and 5d) were doped into four sites: Site I (a W atom position), Site II (a Ge atom position), Site III (a middle-layer N atom position), and Site IV (a surface-layer N atom position). The corresponding configurations are named WGe_2N_4-I@TM, WGe_2N_4-II@TM, WGe_2N_4-III@TM, and WGe_2N_4-IV@TM, respectively. The structures of H adsorbed on TM-doped WGe_2N_4 are shown in Fig. S3. Figure 4(b) shows that ΔG_{*H} values for all WGe_2N_4-I@TM configurations are positive, and their corresponding exchange currents lie in the right portion of the volcano curve (Fig. 4(c)). The most favorable configuration among them is WGe_2N_4-I@Sc with a ΔG_{*H} value of 0.11 eV. For WGe_2N_4-II@TM, the distribution of ΔG_{*H} values is relatively balanced between positive and negative values (Fig. 4(d)). This might be attributed to the fact that shallow doping at Site II exerts a greater influ-

ence on the surface N atoms than deep doping at Site I, thus exerting a stronger modulating effect on HER activity. The ΔG_{*H} value closest to zero for this site is 0.18 eV for WGe_2N_4-II@Tc, slightly larger than that for WGe_2N_4-I@Sc (0.11 eV). Most ΔG_{*H} values for WGe_2N_4-II@TM are obviously deviated from zero. A ΔG_{*H} value deviating significantly from zero results in a lower exchange current, which is detrimental to HER catalytic activity (Fig. 4(e)).

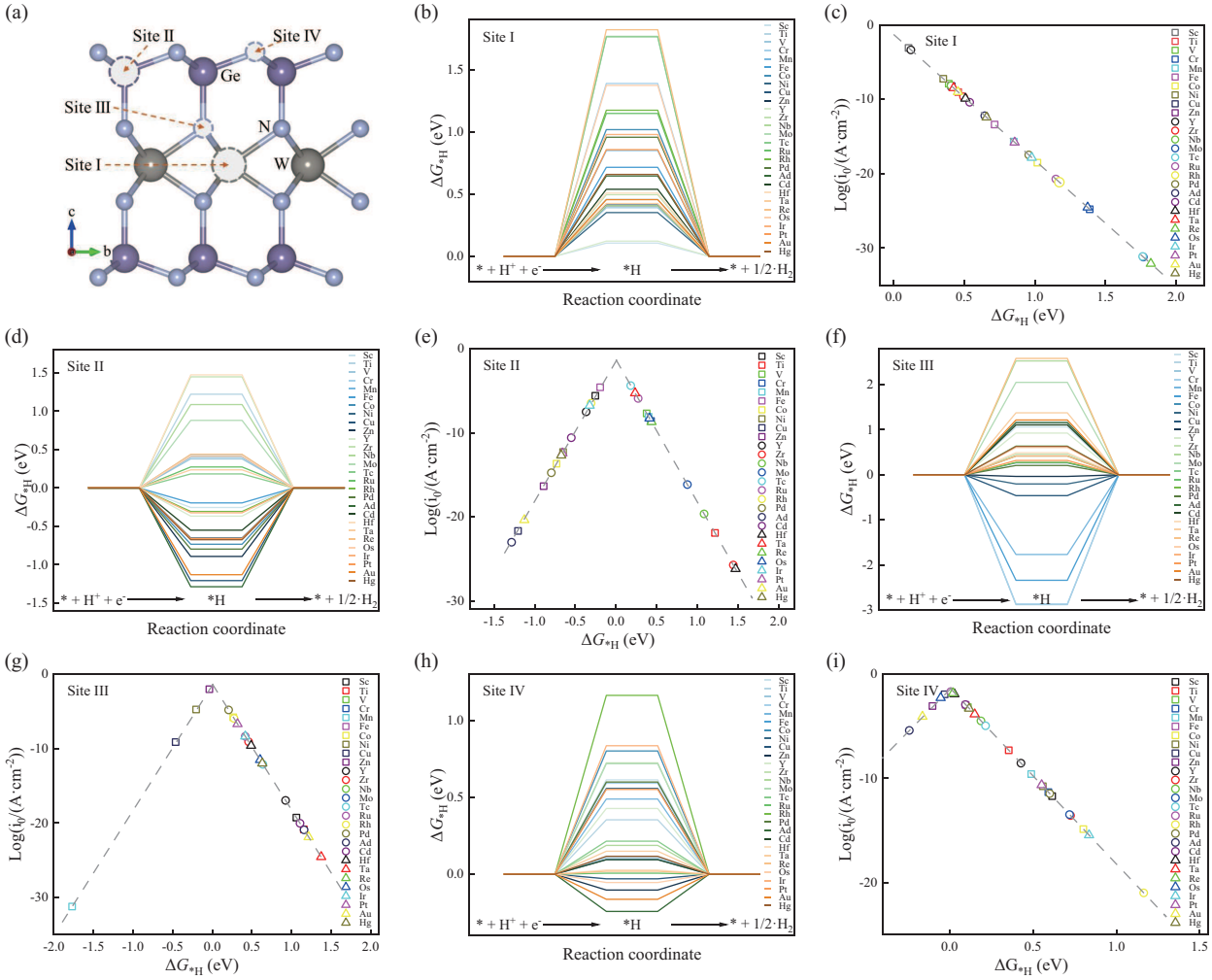


Fig. 4. (a) Schematic structure of WGe_2N_4 with four doping sites. (b) Free energy diagram for HER on WGe_2N_4-I@TM. (c) Calculated volcano curve for WGe_2N_4-I@TM. (d) Free energy diagram for HER on WGe_2N_4-II@TM. (e) Calculated volcano curve for WGe_2N_4-II@TM. (f) Free energy diagram for HER on WGe_2N_4-III@TM. (g) Calculated volcano curve for WGe_2N_4-III@TM. (h) Free energy diagram for HER on WGe_2N_4-IV@TM. (i) Calculated volcano curve for WGe_2N_4-IV@TM.

For WGe_2N_4-III@TM and WGe_2N_4-IV@TM, the transition metal atom substitutes for the N atom. Figure 4(f) shows that most ΔG_{*H} values are positive, with a small proportion being negative. Among all WGe_2N_4-III@TM configurations, WGe_2N_4-III@Zn possesses a ΔG_{*H} value closest to zero of -0.04 eV, superior to those of both WGe_2N_4-I@TM and WGe_2N_4-II@TM configurations. Notably, this value is even better than those of commercial catalysts, such as Pt and Ir.[40,41] Figure 4(g) shows that the exchange current density of WGe_2N_4-III@Zn is close to the peak of the volcano curve, ensuring its performance advantage for HER. As depicted in Fig. 4(h), ΔG_{*H} values for WGe_2N_4-IV@TM exhibit a similar distribution to those of WGe_2N_4-III@TM. Notably, ΔG_{*H} values for some WGe_2N_4-IV@TM configurations, such as WGe_2N_4-IV@Ru (0.01 eV) and WGe_2N_4-IV@Re (0.02 eV), are generally closer to zero than those for WGe_2N_4-III@TM configurations. As a result, exchange current densities for more WGe_2N_4-IV@TM configurations are closer to the volcano peak, suggesting their excellent HER activity (Fig. 4(i)). This effect might be attributed to doping at the surface N site influencing HER activity by modifying the electronic properties of subsurface Ge atoms and thus neighboring surface N atoms. In short, TM doping can effectively activate the HER catalytic activity of WGe_2N_4, and the top ten performing systems based on ΔG_{*H} are WGe_2N_4-IV@Ru (ΔG_{*H} = 0.01 eV) > WGe_2N_4-IV@Re (0.02 eV) > WGe_2N_4-IV@Hf (0.03 eV) > WGe_2N_4-IV@Cu (-0.03 eV) > WGe_2N_4-III@Zn (-0.04 eV) > WGe_2N_4-IV@Os (-0.05 eV) > WGe_2N_4-IV@Cd (0.09 eV) > WGe_2N_4-IV@Fe (0.10 eV) > WGe_2N_4-IV@Zn (-0.10 eV) > WGe_2N_4-I@Sc (0.11 eV). It

should be noted that different dopants can induce local electronic structure variations, which may in principle influence the preferred adsorption site and the resulting HER performance. A detailed, site-specific investigation of the dopants is necessary for future research.

3.6. Chemical bonding mechanism

On the surface of MA_2Z_4 materials, nitrogen undergoes chemisorption with hydrogen. According to molecular orbital theory, this primarily involves hybridization between nitrogen's orbitals and hydrogen's molecular orbitals (Fig. 5(a)). The characteristics and degree of orbital hybridization can elucidate the specific mechanism of this chemisorption reaction. Hence, projection density of states (PDOS) and crystal orbital Hamilton population (COHP) calculations were conducted to further reveal the chemical bonding mechanism between the surface N and H atoms for the top ten configurations. For WGe_2N_4-IV@Ru, the formation of the N–H bond is primarily due to hybridization between the N_{2p_z} and H_{1s} orbitals, as evidenced by their large PDOS overlaps, while the N_{2s} orbital contributes little (Fig. 5(b)). Similarly, the N–H bond in the other nine configurations originates from hybridization between the N_{2p_z} orbital and H_{1s} orbital (Fig. S4). However, little overlap between the N_{2p_z} and H_{1s} orbitals is observed for pristine WGe_2N_4, implying extremely weak hybridization (Fig. 5(c)). Moreover, integrated COHP (ICOHP) calculations were performed to quantify the strength of the N–H bond. Figure 5(d) shows that the –ICOHP values for these ten systems range from 3.61 to 3.77, significantly larger than that for pristine WGe_2N_4 (0.03), in accordance with the PDOS results. Additionally, COHP calculations show that pristine WGe_2N_4 exhibits negligible bonding states compared with these ten systems (Fig. 5(e)). The extremely weak N–H bond in pristine WGe_2N_4 leads to difficult hydrogen atom chemisorption and a large HER energy barrier. In contrast, these ten systems exhibit a remarkable improvement in hydrogen chemisorption, which facilitates HER and results in superior exchange current densities. These results are consistent with the PDOS, ICOHP, ΔG_{*H}, and exchange current density data.

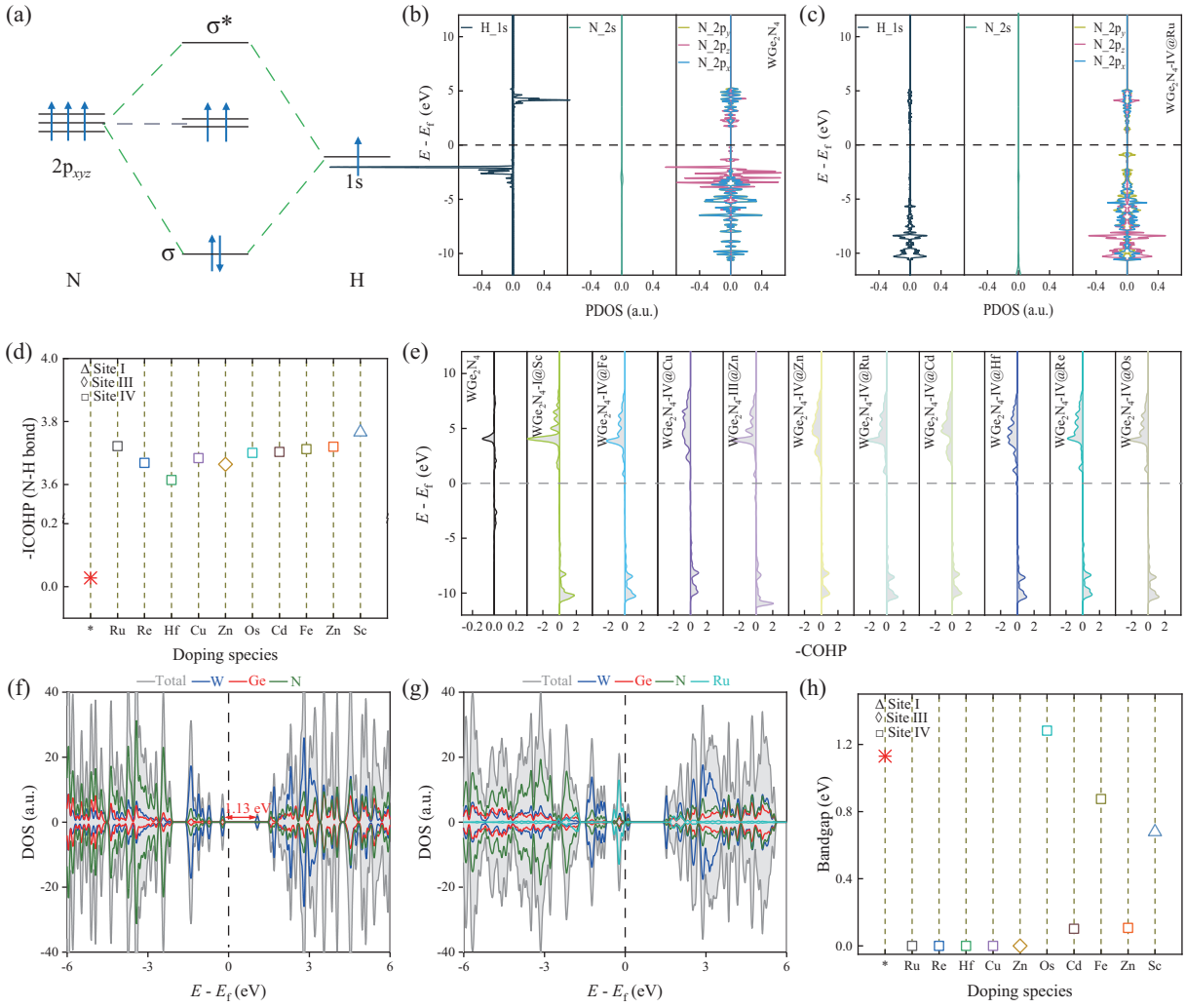


Fig. 5. (a) PDOS for the H_{1s} orbital, N_{2s} orbital, and N_{2p} orbital. (b) The integrated COHP (ICOHP) of the N–H bond for WGe_2N_4 and the doped configurations (WGe_2N_4-IV@Ru, WGe_2N_4-IV@Re, WGe_2N_4-IV@Hf, WGe_2N_4-IV@Cu, WGe_2N_4-III@Zn, WGe_2N_4-IV@Os, WGe_2N_4-IV@Cd, WGe_2N_4-IV@Fe, WGe_2N_4-IV@Zn, and WGe_2N_4-I@Sc). (c) COHP for these ten configurations. (d) Electronic density of states of WGe_2N_4-IV@Ru. (e) Bandgaps for these ten configurations.

3.7. Improving electronic conductivity

Then, the electronic structures of the top ten systems were analysed using first-principles calculations. As shown in Fig. 5(f), WGe_2N_4 exhibits a semiconducting characteristic with a bandgap of 1.13 eV. In contrast, WGe_2N_4-IV@Ru (Fig. 5(g)), WGe_2N_4-IV@Re, WGe_2N_4-IV@Hf, WGe_2N_4-IV@Cu, and WGe_2N_4-III@Zn exhibit metallic behavior, as evidenced by bands crossing the Fermi level (Fig. S5), demonstrating superior electronic conductivity. However, WGe_2N_4-IV@Os, WGe_2N_4-IV@Cd, WGe_2N_4-IV@Fe, WGe_2N_4-IV@Zn, and WGe_2N_4-I@Sc are semiconductors with bandgaps of 1.28 eV, 0.10 eV, 0.88 eV, 0.11 eV, and 0.68 eV, respectively (Figs. S5 and 5(h)). Compared with pristine WGe_2N_4, the bandgaps of nine systems (except WGe_2N_4-IV@Os) are reduced, suggesting better electronic conductivity. In contrast, the bandgap of WGe_2N_4-IV@Os increases, which might be attributed to enhanced band hybridization between the W and N atoms induced by the Os dopant.

3.8. Stability of dopants

To verify the dynamic stability of dopants, we performed AIMD simulations for three representative dopants (WGe_2N_4-I@Sc, WGe_2N_4-III@Zn, and WGe_2N_4-IV@Ru) with different doping sites, namely the W site, inner N site, and surface N site. The total mean squared displacements (MSDs) from AIMD at 300 K for 5000 fs show that the MSDs for W, Ge, N, and Sc atoms approach zero, indicating the dynamic stability of WGe_2N_4-I@Sc (Fig. 6(a)). However, WGe_2N_4-III@Zn shows obvious MSDs for Ge and Zn atoms, implying dynamic instability (Fig. 6(b)). For WGe_2N_4-IV@Ru, the MSD of the Ru atom exhibits a small displacement and then stabilizes, while no significant MSD is observed for other atoms, suggesting its dynamic stability (Fig. 6(c)). The initial and final structures for WGe_2N_4-I@Sc, WGe_2N_4-III@Zn, and WGe_2N_4-IV@Ru are shown in Figs. 6(d), 6(e), and 6(f), respectively. For WGe_2N_4-III@Zn, a Ge atom diffuses from the subsurface to the surface, while the Zn atom migrates from the inner N site to the Ge vacancy site, resulting in the large MSD. The other two material atoms show no significant displacement. This observation is consistent with the MSD results. Based on the above results, doping transition metals at Site I is the most stable, followed by doping at Site IV, while doping at Site III is unstable. This finding provides valuable reference and guidance for studying transition metal doping in MA_2N_4 materials for material modification.

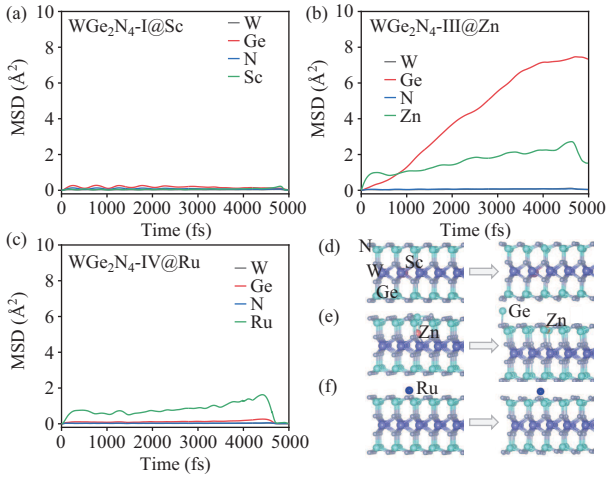


Fig. 6. The total MSDs for (a) WGe_2N_4-I@Sc, (b) WGe_2N_4-III@Zn, and (c) WGe_2N_4-IV@Ru from AIMD simulations at 300 K for the last 5000 steps with 1 fs per step. The initial and final states for (d) WGe_2N_4-I@Sc, (e) WGe_2N_4-III@Zn, and (f) WGe_2N_4-IV@Ru before and after AIMD simulations. The left is the initial state, and the right is the final state.

4. Conclusion

In summary, this work presents a systematic screening of potential HER catalysts from among 2D MA_2Z_4 materials and proposes activation strategies for inert systems. Six promising systems were screened from 48 candidates based on their excellent HER activity, as indicated by ΔG_{*H} and exchange current density. Doping strategies can effectively activate the HER activity of the inert material WGe_2N_4, and ten systems were identified with ΔG_{*H} values close to zero. In particular, the ΔG_{*H} value for WGe_2N_4-IV@Ru is only 0.01 eV. Additionally, the N–H bonding mechanism has been elucidated to deepen the understanding of HER on these materials. These results significantly advance the study of 2D MA_2N_4 materials as HER catalysts and promote their potential applications. A deeper mechanistic understanding of how atomic composition, crystal structure, and electronic structure collectively govern catalytic performance remains a vital goal for subsequent research. Unravelling these complex interactions is key to translating fundamental knowledge into practical design rules for the screening and engineering of high-performance MA_2Z_4 catalysts.

Acknowledgments

Project supported by the National Natural Science Foundation of China (Grant No. 12304084) and the Natural Science Foundation of Jiangsu Province (Grant No. BK20220930).

References

[1] Kempler P A, Coridan R H and Luo L 2024 *Chem. Rev.* **124** 10964
[2] Wu Y, Xu G, Zhou J and Cao D 2025 *Chem. Eng. J.* **505** 159291
[3] Gao T, An Q, Tang X, Yue Q, Zhang Y, Li B, Li P and Jin Z 2024 *Phys. Chem. Chem. Phys.* **26** 19606
[4] Zhang H, Liu Z, Fang L, Wang Y, Chen S and Ren W 2025 *Chin. Phys. B* **34** 086109
[5] Ren J T, Chen L, Wang H Y, Tian W W and Yuan Z Y 2024 *Energy Environ. Sci.* **17** 49
[6] Tüysüz H 2024 *Acc. Chem. Res.* **57** 558
[7] Wang P, Zheng J, Xu X, Zhang Y Q, Shi Q F, Wan U, Ramakrishna S, Zhang J, Zhu L, Yokoshima T, Yamauchi Y and Long Y Z 2024 *Adv. Mater.* **36** 2404806

[8] Feidenhans'l A A, Regmi Y N, Wei C, Xia D, Kibsgaard J and King L A 2024 *Chem. Rev.* **124** 5617

[9] Voiry D, Yamaguchi H, Li J, Silva R, Alves D C B, Fujita T, Chen M, Asefa T, Shenoy B B, Eda G and Chhowalla M 2015 *Nat. Mater.* **12** 850

[10] Deng J, Li H, Xiao J, Tu Y, Deng D, Yang H, Tian H, Li J, Ren P and Bao X 2015 *Energy Environ. Sci.* **8** 1594

[11] Yang Y Y, Pan F C, Li J L, Gong F, Hu J, Zheng Q, Lin D and Huo Y 2025 *J. Colloid Interface Sci.* **685** 196

[12] She Z W, Fredrickson K D, Anasori B, Kibsgaard J, Strickler A L, Lukatskaya M R, Gogotsi Y, Jaramillo T F and Vojvodic A 2016 *ACS Energy Lett.* **1** 589

[13] Zeng Z, Chen X, Weng K, Wu Y, Zhang P, Jiang J and Li N 2021 *npj Comput. Mater.* **7** 80

[14] Zhao Y, Zhang J, Guo X, Cao X, Wang S, Liu H and Wang G 2023 *Chem. Soc. Rev.* **52** 3215

[15] Wang X, Maeda K, Thomas A, Takanabe K, Xin G, Carlsson J M, Domen K and Antonietti M 2009 *Nat. Mater.* **8** 76

[16] Hong Y L, Liu Z, Wang L, Zhou T, Ma W, Xu C, Feng S, Chen L, Chen M L, Sun D M, Chen X Q, Cheng H M and Ren W 2020 *Science* **369** 670

[17] Wang L, Shi Y, Liu M, Zhang A, Hong Y L, Li R, Gao Q, Chen M, Ren W, Cheng H M, Li Y and Chen X Q 2021 *Nat. Commun.* **12** 2361

[18] Guo S D, Zhu Y T, Mu W Q and Ren W C 2020 *Europhys. Lett.* **132** 57002

[19] Tian M, Wei C, Zhang J, Wang J and Yang R 2021 *Phys. Rev. B* **103** 195305

[20] Guo S D, Mu W Q, Wang J H, Yang Y X, Wang B and Ang Y S 2022 *Phys. Rev. B* **106** 064416

[21] Wei F, Jia B, Gao J, Zhao J, Yang F, Chen F, Yuan Y, Zhang C, Hao J and Lu P 2024 *Int. J. Hydrogen Energy* **61** 528

[22] Zhou T, Xu C and Ren W 2025 *Nat. Rev. Mater.* **10** 907

[23] Zheng J, Sun X, Hu J, Wang S, Yao Z, Deng S, Pan X, Pan Z and Wang J 2021 *ACS Appl. Mater. Interfaces* **13** 50878

[24] Zang Y, Wu Q, Du W, Dai Y, Huang B and Ma Y 2021 *Phys. Rev. Mater.* **5** 045801

[25] Qian W, Chen Z, Zhang J and Yin L 2022 *J. Mater. Sci. Technol.* **99** 215

[26] Xiao C, Sa R, Cui Z, Gao S, Du W, Sun X, Zhang X, Li Q and Ma Z 2021 *Appl. Surf. Sci.* **563** 150388

[27] Ding Y and Wang Y 2023 *Appl. Surf. Sci.* **627** 157256

[28] Liu Y, Ji Y and Li Y 2021 *J. Phys. Chem. Lett.* **12** 9149

[29] Kresse G and Furthmüller J 1996 *Phys. Rev. B* **54** 11169

[30] Blöchl P E 1994 *Phys. Rev. B* **50** 17953

[31] Grimme S, Antony J, Ehrlich S and Krieg H 2010 *J. Chem. Phys.* **132** 154104

[32] Nørskov J K, Bligaard T, Logadottir A, Kitchin J R, Chen J G, Pandelov S and Stimming U 2005 *J. Electrochem. Soc.* **152** J23

[33] Dronskowski R and Blöchl P E 1993 *J. Phys. Chem.* **97** 8617

[34] Momma K and Izumi F 2011 *J. Appl. Crystallogr.* **44** 1272

[35] Baroni S, de Gironcoli S, Corso A D and Giannozzi P 2001 *Rev. Mod. Phys.* **73** 515

[36] Laursen A B, Varela A S, Dionigi F, Fanchiu H, Miller C, Trinhammer O L, Rossmeisl J and Dahl S 2012 *J. Chem. Educ.* **89** 1595

[37] Gao G, Zhu G, Chen X, Sun Z and Cabot A 2023 *ACS Nano* **17** 20804

[38] Hinnemann B, Moses P G, Bonde J, Jørgensen K P, Nielsen J H, Horch S, Chorkendorff I and Nørskov J K 2005 *J. Am. Chem. Soc.* **127** 5308

[39] Song X L, Chen L, Gao L J, Ren J T and Yuan Z Y 2024 *Green Energy Environ.* **9** 166

[40] Li C and Baek J B 2020 *ACS Omega* **5** 31

[41] Ma W, Zhang X, Li W, Jiao M, Zhang L, Ma R and Zhou Z 2023 *Nanoscale* **15** 11759